

NASA Technical Memorandum 103285

Optical Measurement of Unducted Fan Flutter

(NASA-TM-103285) OPTICAL MEASUREMENT OF
UNDUCTED FAN FLUTTER (NASA) 11 p CSCL 21E

N91-15174

Unclass
G3/07 0320483

Anatole P. Kurkov and Oral Mehmed
*Lewis Research Center
Cleveland, Ohio*

Prepared for the
Thirty-sixth International Gas Turbine and
Aeroengine Congress and Exposition
sponsored by the American Society of Mechanical Engineers
Orlando, Florida, June 3-6, 1991

NASA

OPTICAL MEASUREMENTS OF UNDUCTED FAN FLUTTER

Anatole P. Kurkov and Oral Mehmed
National Aeronautics and Space Administration
Lewis Research Center
Cleveland, Ohio 44135

ABSTRACT

The paper describes a nonintrusive optical method for measuring flutter vibrations in unducted fan or propeller rotors and provides detailed spectral results for two flutter modes of a scaled unducted fan. The measurements were obtained in a high-speed wind tunnel. A single-rotor and a dual-rotor counterrotating configuration of the model were tested; however, only the forward rotor of the counterrotating configuration fluttered. Conventional strain gages were used to obtain flutter frequency; optical data provided complete phase results and an indication of the flutter mode shape through the ratio of the leading- to trailing-edge flutter amplitudes near the blade tip. In the transonic regime the flutter exhibited some features that are usually associated with nonlinear vibrations. Experimental mode shape and frequencies were compared with calculated values that included centrifugal effects.

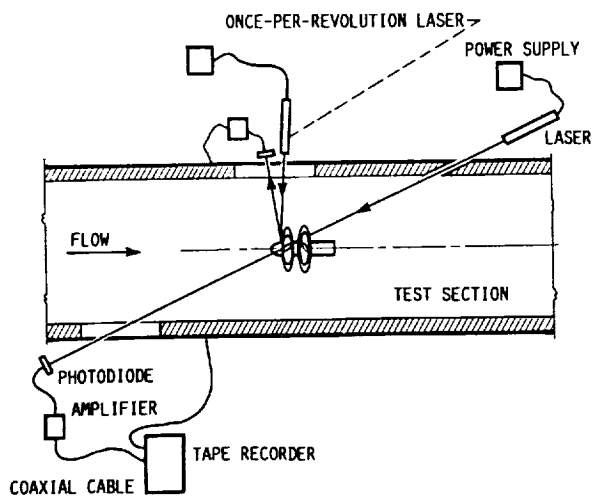


Figure 1.- Test schematic.

INTRODUCTION

Optical measurement of flutter vibrations (Nieberding and Pollack, 1977) has been used in turbomachinery for a number of years. However, because this method requires the proximity of a wall next to the blade tips, it is unsuitable for Unducted Fans and propellers. To measure the steady-state deflections for these rotors, Kurkov (1988; 1989) applied another method in which a laser beam is directed across the rotational plane to a photodetector. As illustrated in Fig. 1, the laser and the detector are positioned remotely so that they do not interfere with the flow. As the beam is chopped by the rotor, a series of pulses are generated (Fig. 2). These pulses are indicative of the instantaneous positions of the blades.

The paper illustrates the use of this method to measure unsteady displacements during flutter of an unducted fan model installed in a high-speed wind tunnel. Because of the complexity of the flutter in the transonic region, additional information provided by the displacement data was essential for interpreting flutter modes.

Beyond the flutter instrumentation aspects, the paper presents new experimental data in the transonic flutter regime for a composite unducted fan model rotor. Particular attention is placed on reporting features that, in general, are associated with nonlinear vibrations, since the nonlinear aspects of flutter

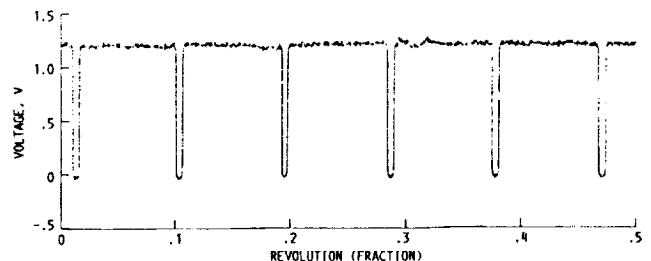


Figure 2.- Blade-tip pulses.

in the transonic region are of current interest. Bendiksen (1990) has presented some results obtained by a simultaneous solution of nonlinear aerodynamic and structural equations. The flutter mode arrived at by Bendiksen is essentially chordwise bending with the strong participation of the trailing edge.

Most of the results that are relevant for comparison with theoretical solutions are presented in the section entitled "Flutter Modes." The more detailed results presented in the section entitled "Flutter Spectra" illustrate some of the dynamic aspects of flutter as well as techniques used in the analysis. Therefore, the material in this section should also be of interest to the data analyst.

Following the usual practice, the performance and blade element parameters in this report were calculated by using the free-stream conditions. However, for accurate comparison with theoretical results, these parameters should be adjusted for the axial flow acceleration due to the nacelle forebody. Experimental data of Podboy and Krupar (1989) obtained with the same nacelle and similar blades indicate that the axial velocity at the tip increased by about 6.5 percent of the free-stream velocity.

EXPERIMENTAL MEASUREMENTS

The same equipment can be used to measure the steady-state deflections (Kurkov, 1988) and the flutter vibrations. The only difference is that the steady-state deflections remain essentially constant for every revolution whereas vibratory deflections vary (excluding the integral engine-order vibrations). The steady-state component of the signal is obtained by averaging

blade pulse times measured with respect to the once-per-revolution pulse over a number of revolutions (typically about 100). The dynamic pulse-displacement times are obtained by subtracting the averaged steady-state times from the original pulse times.

The geometry of deflection measurement in the plane perpendicular to the blade pitch (Z) axis, is given in Fig. 3. The coordinate system in this figure is fixed with respect to the undeflected blade, and therefore, the laser beam is rotated relative to the undeflected blade to depict the intersection of the beam and the deflected blade. The experimentally measured displacements are along the arc (centered with respect to the rotational axis) subtended by the vector d_t (Fig. 3). The geometrical relationships for various degrees of approximations are given by Kurkov (1988). The relationships still hold for a single-degree-of-freedom flutter, provided that either the instantaneous dynamic deflection or the vibratory amplitude is substituted for the steady-state deflection.

In this paper deflections are left essentially in the same form as they are defined in the experiment. Therefore, for comparison with experimental data, the calculated displacements along the major axes are used to derive the displacements that are equivalent to the experimentally measured displacements as shown in Fig. 3.

In the experiment only the forward rotor fluttered. Therefore, during the alignment of the laser beam it was necessary to bypass the rear rotor by tilting it slightly toward the axis. It was also desirable to intersect a blade with the laser beam in the plane approximately perpendicular to the pitch axis and to form some small positive incidence angle γ relative

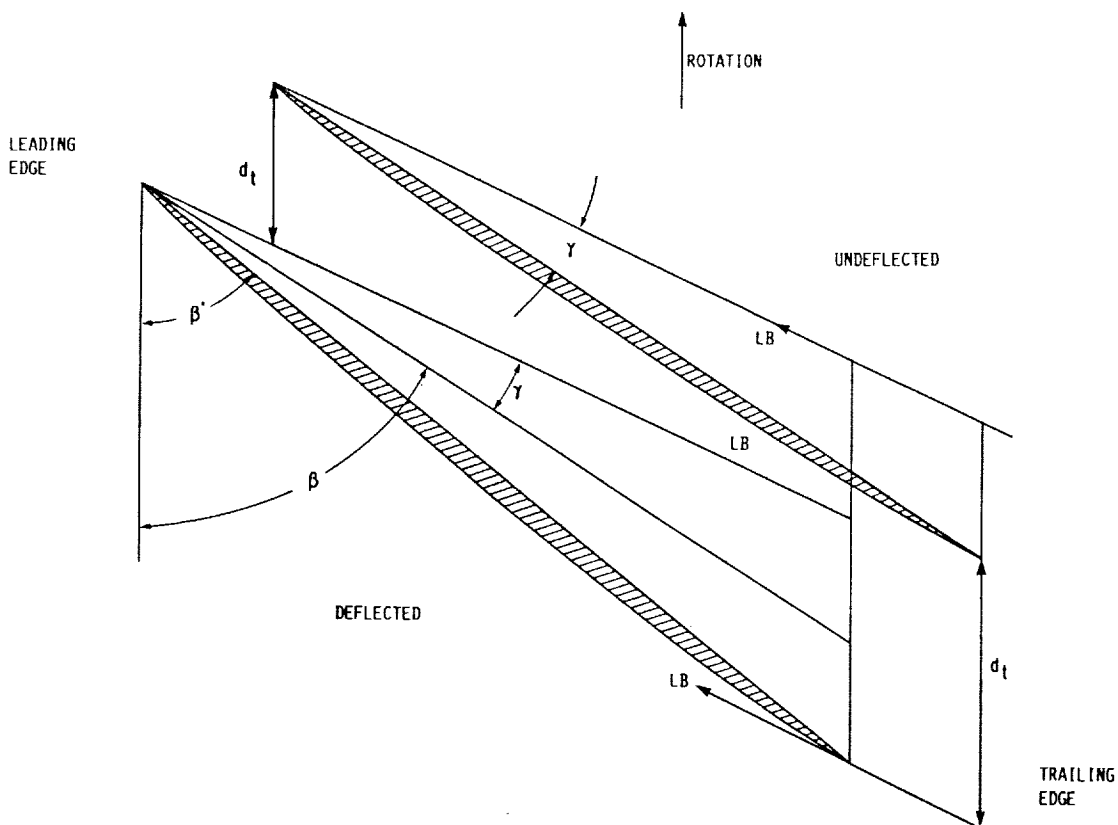


Figure 3.- Geometry of laser beam and blade section; d_t denotes measured deflection; γ denotes laser beam incidence; β' and β denote deflected and undeflected blade angles.

to the blade chord in the plane of intersection. These requirements could be satisfied provided that the blade-beam intersection occurred somewhat past the 12 o'clock position (facing the rotor). The beam intersection time was minimized by focusing the beam on the intersecting blade. Optical line filters were used to cut down the extraneous light. The silicon photodiode detector and the amplifier were manufactured by United Detector Technology, and the helium-neon laser by Aerotech.

The displacement data were recorded during the test on a magnetic tape by using a frequency-modulated wideband II magnetic recorder (Honeywell 101). The frequency bandwidth was 500 kHz. The desired real-time digitizing speed was achieved by reducing the tape speed on playback. A Concurrent computer model 5450 was used to digitize and process the data.

Since the displacement data were digitized at a near constant rate of 12 000 points per revolution, it was convenient to express absolute displacements in digitized units (i.e., in $1/12000^{\text{th}}$ of the revolution fraction). Similarly, in most cases it was convenient to express frequency in engine orders E, since in this way a clear distinction is made between the forced response and the self-excited vibrations.

Figure 4 illustrates the blade planform and the first three natural modes calculated for a stationary blade in a vacuum. The calculated frequencies are also given in the figure. The blade was designed by General Electric as one of the model blades (designated F21) for its Unducted Fan engine. It has a graphite/glass shell and a half-span titanium spar. Tip diameter is 61.8 cm and tip sweep angle is 45° . There were 13 blades on the forward and 10 on the aft rotor. More information on this and related blades and tests is available (Balan, et al., 1988).

At the time of these tests there were three active strain gages on the forward rotor on three different blades (denoted as channels 4, 6, and 12). These gages were mounted near a blade tip and were sensitive to twist deformation and rather insensitive to bending.

Except for the windmill points, flutter was approached for a set wind tunnel Mach number by increasing rotational speed. For the windmill points flutter was approached by increasing the tunnel Mach number. These steps were reversed to get out of flutter. The shutdown was triggered automatically when the stress limit was exceeded, except for windmill points, when it was performed manually.

FLUTTER MODES

As already mentioned, there were two distinct flutter modes. During the preliminary analysis of the

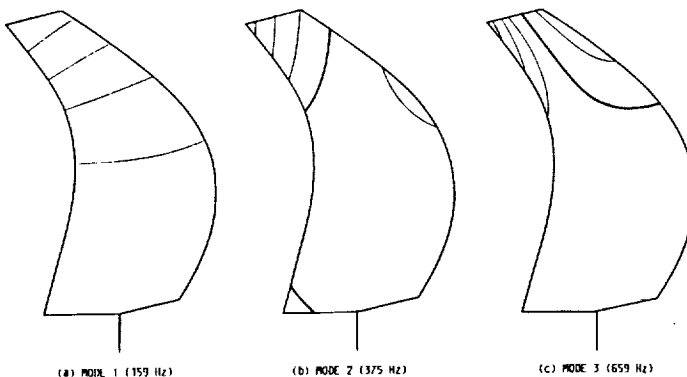


Figure 4.- Nonrotating blade mode shapes.

flutter data, it became apparent that in the higher frequency mode flutter occurred over a fairly wide frequency range. In order to examine the reason for this variation, the subsequent flutter points were selected so that they spanned the full observed frequency range. Some of the points selected for the detailed analysis were from the dual-rotor tests. As a rule, however, the data from the single-rotor tests were favored.

Figure 5 presents the Campbell diagram that includes all the data points discussed in this report; however, no distinction is made between the dual and the single rotor tests. The frequencies for the first two modes were calculated for the blade setting angle of 58° . In order to illustrate variations in frequencies with the blade setting angle, two points for $\beta = 55^\circ$ and 61.2° were also included.

The displacement spectral results were available for both the leading and trailing edges at a near-tip span. Consequently, by taking the ratio of the leading- to trailing-edge flutter amplitudes, an indication of the flutter mode shape could be obtained. This ratio was also calculated from the natural mode shape for the associated mode. The calculated natural mode shape included the centrifugal effects, but it did not include the effect of added mass due to air density or the modification of the deflected shape due to air loads.

In order to properly locate the two points in the finite element model that correspond to the intersection of the laser beam and the blade contour in the experiment, a similar procedure as for the steady-state deflections (Kurkov, 1988) was adopted. The deflected points were obtained by intersection of a line representing the laser beam and the deflected contours of the leading and trailing edges. Two deflected shapes were considered. The first one included only the centrifugal steady-state deflections. The second one included both the centrifugal and modal deflections represented by the vibratory amplitude. In order to approximate the experimental conditions the modal deflections were scaled so that they were small relative to the centrifugal. The simulated experimental modal amplitudes were obtained as the difference between the tangential displacements (d_t in Fig. 3) associated with the second and first deflection calculations. (Note that both deflection calculations were

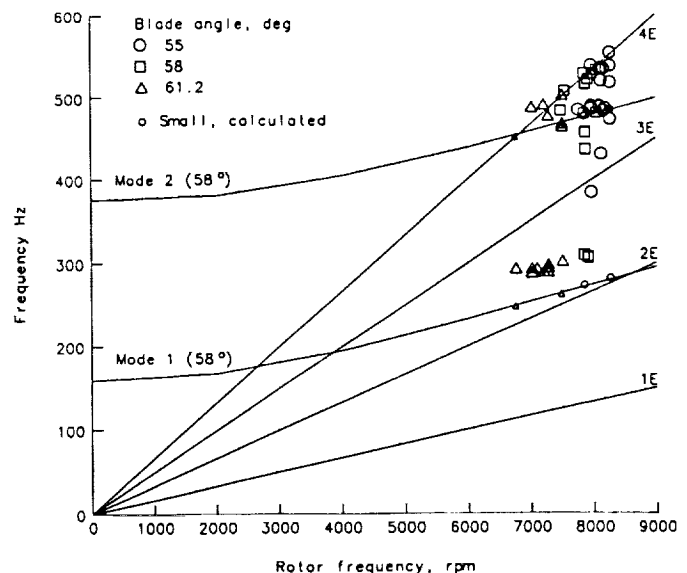


Figure 5.- Campbell diagram.

evaluated relative to the undeflected finite element blade contour.) Because most of the steady-state deflection for these blades was caused by centrifugal forces, and because the agreement between the calculated and measured deflections for the particular blade was good (Kurkov, 1988), this procedure should give a good representation of the equivalent experimental leading- to trailing-edge amplitude ratio.

Modal ratio results are presented in Fig. 6. The calculated results are shown by the large open symbols. (In Fig. 5 they were shown by small open symbols.) They were obtained for the two extreme blade setting angles β of 55° and 61.2° and for the rotational speeds that span the experimental range for the associated blade angles. Thus they illustrate calculated variation in frequencies and modal ratio for the experimental range of rotational speeds and blade angles. Also noted in the figure are the predominant nodal diameters associated with each point. They were obtained from the overall displacement spectra as described in the next section.

The cluster of points near the first natural frequency appears to be associated with the single-degree-of-freedom flutter mode, since both the frequency and the mode shape deviate by a relatively small amount from the calculated values for the first mode. This differs from previous experience with another advanced propfan composite model, where the experimental flutter frequencies were between the first two natural modes (Mehmed and Kaza, 1986; Kaza et al., 1987). Note that the second mode for these blades was mainly torsion, rather than second bending as for the current blades. The experimental flutter frequency for a composite blade reported by Crawley and Ducharme (1989) was also between the first two in-vacuum natural modes; however, the second mode for this blade was second bending.

Predominant nodal diameters for this group of points in Fig. 6 range from -3 to -6. The slight shift in frequencies is of the order of the variation caused by the change in the rotational speed or the blade setting angle β , as shown by the large open symbols. The solid symbols correspond to the dual-rotor configuration.

Although most of the plotted points in Fig. 6 are associated with the primary response (or the dominant peak), some points associated with the secondary

response (or minor peaks) were also plotted. Therefore, this figure also includes some points for which the stress level was relatively low, of the order of 2 kN/cm² rather than the 4 to 6 kN/cm² for most of the flutter points. This permitted a more complete documentation of all the modes and frequencies and revealed some of the changes in response with deeper penetration into the flutter region. (Note that the current flutter theories can only deal with flutter inception.)

The second group of points in Fig. 6 is clustered to the right and slightly below the second natural mode. This mode has a nodal line near the tip as shown in Fig. 4. As a result, the displacement of the trailing edge is much higher than that of the leading edge. The phase angle in both the experimental and calculated displacements is such that the center of rotation is in front of the leading edge. The spread in frequency for this mode is larger than can be attributed to the speed or the blade setting angle variation. The frequency spread is particularly large for the -2 nodal diameter. It is 64 Hz, which is about twice what would be expected from a calculated in-vacuum frequency variation for the range of experimental variables. Note, however, that in the experiment circles fall to the right of triangles, Fig. 6, as predicted by the in-vacuum modes. The mode shape for all points is reasonably close to the calculated shape, particularly taking into account the fact that the displacement amplitude at the leading edge is fairly small and, therefore, may not be accurate.

The response away from the immediate vicinity of the two natural frequencies is, in general, secondary and of low stress or displacement amplitude level. However, it does illustrate the rather wide possible range of nonintegral-order, self-excited vibrations in the transonic flow regime. These points correspond to positive nodal diameters of 2 and 3. Only one of these points, the 3-nodal-diameter, $\beta = 61.2^\circ$ point with the amplitude ratio of 0.2, is near the natural mode. (Note that without the knowledge of amplitude ratio, the group of points with positive nodal diameters would not stand out from the zero and negative nodal diameter points clustered around the second natural mode.)

The frequency spread of the higher flutter mode was examined further by plotting the tip relative Mach numbers for these points in terms of frequency in Fig. 7 and in terms of advance ratio J in Fig. 8. (Advance ratio J is defined as the ratio of the free-stream axial velocity and a product of the rotational frequency n and the tip diameter D .) Below a relative Mach number of about 0.98, the predominant response is the 0-nodal-diameter mode with some secondary response at the -1 mode at frequencies about 50 Hz higher. Above the relative Mach number of 0.98, the -2-nodal-diameter mode appears at the high end of the frequency range. The frequency gap evident in Fig. 7 at low relative Mach numbers is ultimately closed by the -2-nodal-diameter points at the high limit of the relative Mach number. Despite this frequency spread for different nodal diameters and relative Mach numbers, the flutter data correlate fairly well in Fig. 8, where the independent variable is the advance ratio J , which is essentially a measure of the relative flow angle. For a given value of J , the higher value of the blade setting angle corresponds to a higher incidence. The two points that seem to deviate from the others illustrate the incidence effect on the flutter. The square, corresponding to a blade setting angle of 58° at $J = 2.6$, indicates a drop in the flutter boundary because of the high incidence (it is the low end of J for this value of β), and the circle, corresponding to a blade setting angle of 55° at $J = 2.94$ indicates a

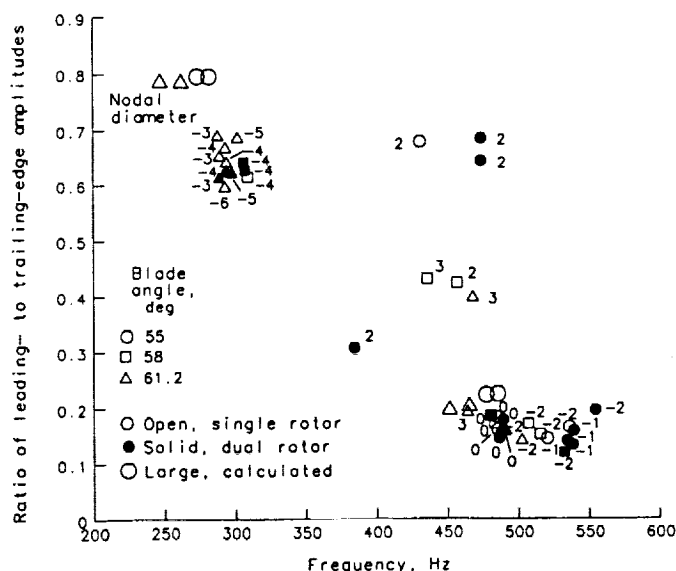


Figure 6.- Ratios of leading - to trailing-edge flutter amplitude and nodal diameters.

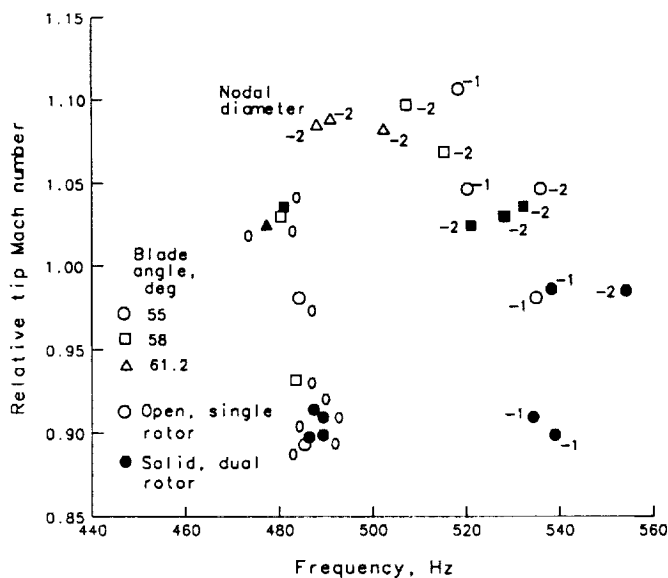


Figure 7.- Relative tip Mach numbers and nodal diameters for second flutter mode.

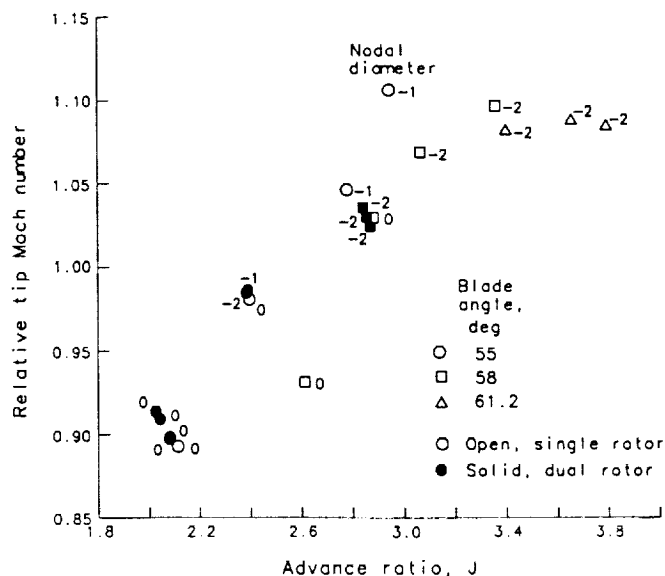


Figure 8.- Second-flutter-mode stability boundary.

rise in the flutter boundary because of the low incidence (it is the high end of J for this β).

During the spectral analysis of the displacement data, it was noticed that for a number of flutter points associated with the higher flutter frequencies the flutter frequency fell close to a four-engine-order response. However, none of these points have the -4-nodal-diameter phase relationship that is necessary for the 4 E forced response mode. In Fig. 9 the data from Fig. 8 are plotted in terms of engine-order frequency. However, since the 0-nodal-diameter points are clustered in a narrow frequency range in Fig. 8, they were not included in Fig. 9. (They would scatter in the range from 3.55 E to 3.88 E in Fig. 9.) Except for the two highest Mach number points (which were the windmill points) for β of 55° and 61.2° with nodal diameters of -1 and -2, respectively, and the -1-nodal-diameter, $\beta = 55^\circ$ point at 3.84 E, all the points cluster within 0.1 E of the 4 E frequency. However, on the whole, the frequency spread for the -1-nodal-diameter, $\beta = 55^\circ$ points in Fig. 9 is not narrower than that in Fig. 7. It appears, therefore, that the response for this mode may be unrelated to the 4 E excitation.

The two right-most points in Fig. 9 for $\beta = 61.2^\circ$ and -2 nodal diameters, which are farthest from the 4 E frequency, are reasonably close to the lower-frequency (about 485 Hz), 0-nodal-diameter cluster of points in Fig. 7. However, the remaining -2-nodal-diameter points, which are associated with the higher frequency range in Fig. 7, are all closely clustered about the 4 E line in Fig. 9. This suggests a possible interaction between the -2-nodal-diameter mode and the 4 E response which is only possible for nonlinear vibrations. This should also warrant some caution when interpreting flutter frequency close to an observed integral engine-order response.

The stability boundary for the first flutter mode is presented in Fig. 10. For $\beta = 58^\circ$, and for the highest Mach number point for $\beta = 61.2^\circ$, the response in the first flutter mode was secondary to the response in the second flutter mode. For the point corresponding to the highest J ($\beta = 61.2^\circ$ windmill), the spontaneous amplitude growth was simultaneous for both flutter modes. The part of the flutter boundary formed by these points is marked by m2 (i.e., second mode)

in Fig. 10. Flutter strictly associated with the first mode occurred in a narrow range of J . As for second-mode flutter, the effect of incidence was destabilizing. A large increase in mistuning was noticed for the lowest Mach number (or the highest incidence) point.

The reduced frequency based on the semichord at 80 percent of the span was in the range 0.2 to 0.22 for the first flutter mode and 0.34 to 0.41 for the second.

FLUTTER SPECTRA

The spectral analysis of data obtained in a stationary reference frame, such as the flutter displacement data, was documented previously (Kurkov, 1984), and hence, only a brief overview is given here. One of the features of the displacement data is that the sampling rate cannot be varied arbitrarily as it is fixed by the rotational speed and the number of blades. Since the flutter frequency is usually greater than the rotational frequency, if each individual blade is analyzed separately, the resulting spectra will be folded several times in the region to the left of $1/2$ E frequency. On the other hand, if all the blades are included as they are sampled, the sampling rate per revolution is then equal to the number of blades, and the folding frequency, expressed in engine orders, is increased to half the number of blades. This sampling method is therefore the choice method in most cases and was used in this study.

The other feature of the displacement spectra is that the observed frequency associated with flutter is shifted away from the true flutter frequency by an exact multiple of engine orders. This shift, expressed in engine orders, is equal to the nodal diameter wave of the flutter mode. The shift is to the right for positive nodal diameters and to the left for negative.

The spectral analysis of the displacement data was optimized by selecting a nearly integral number of cycles in the time domain. This was possible because of the use of Singleton's (1969) algorithm. For the most part, no such optimization was carried out for the strain gage spectra. In order to facilitate the comparison with the displacement spectra, only the low end of the strain gage spectra was displayed.

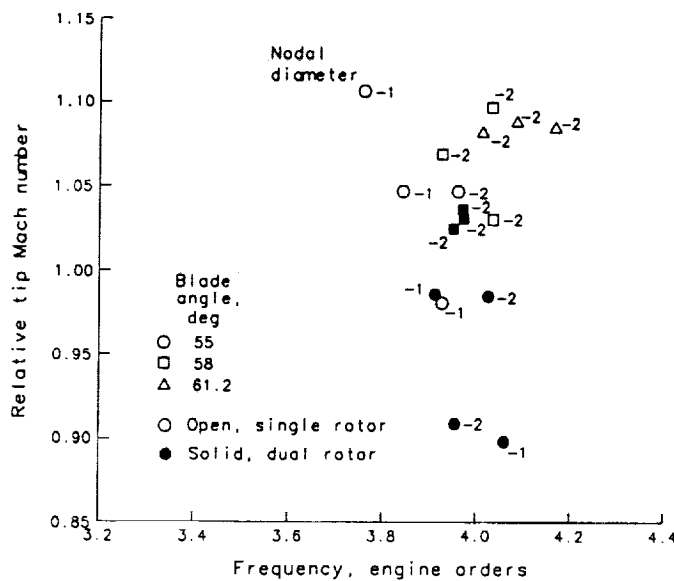


Figure 9.- High-frequency branch of second flutter mode expressed in engine orders.

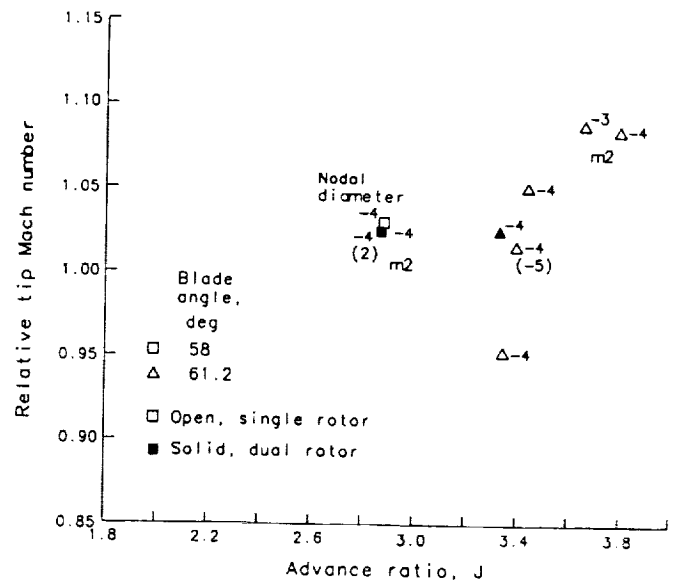


Figure 10.- First-flutter-mode stability boundary.

In this test, the frequency was determined from the strain gage spectra. With the frequency known, the displacement spectra yielded the nodal diameters associated with the flutter mode. Several nodal diameters associated with a single flutter frequency signify mistuning (Whitehead, 1966). The flutter amplitude and phase distribution around the rotor in this case are nonuniform and must be obtained by superposition of several nodal diameter modes.

Note that the integral order response cannot be detected in the displacement spectra because of the nature of the sampling process. Hence all the responses in these spectra, in the absence of any sources, are associated with self-excited vibrations.

The next several figures illustrate the flutter history for the point in Fig. 7 with a frequency of 502.3 Hz, a relative Mach number of 1.081, and $\beta = 61.2^\circ$. The strain gage and displacement spectra of fully developed flutter corresponding to 7512 rpm and a tunnel Mach number of 0.8 are given in Figs. 11 and 12. In order to illustrate the difference in the flutter displacement amplitudes at the leading and trailing edges, both spectra are plotted in Fig. 11. The stress in Fig. 12 was normalized with respect to

the highest peak, 7.14 kN/cm² (dashed line). Unless stated otherwise, when referring to Fig. 12 the solid curve corresponding to N ($N = 8192$) points is implied.

The flutter peak at 4.012 E or 502.3 Hz in the strain gage spectrum (Fig. 12) is shifted by 2 E to the left in the displacement spectrum (Fig. 11). Such a shift implies (Kurkov, 1984) that the mode is -2 nodal diameters. The two peaks in Fig. 11 at 6.26 and 6.29 E correspond to 3.74 and 3.71 E (or 468.3 and 464.3 Hz) peaks in Fig. 12. The fact that the fractional parts of the corresponding engine-order frequencies in these two figures add up to 1 indicates that the two peaks in the displacement spectrum are folded about 6.5 E (or one-half the number of samples per revolution). Taking into account folding, the frequency shift for these two peaks relative to the strain gage spectrum is 3 E and, therefore, they correspond to 3 nodal diameters. The strain gages are less sensitive to these modes than the displacements (Fig. 11) compared with the 502.3 Hz mode. In fact, if the displacement data were not available, these modes would probably be overlooked.

Figure 13 presents the displacement spectrum obtained for a slightly lower rotational speed of 7505.6 rpm. (The tunnel Mach number was 0.8, the same

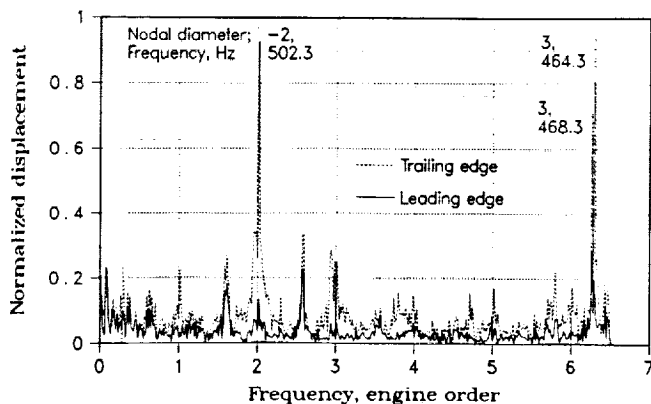


Figure 11.- Displacement spectra at 7512 rpm: blade setting angle, β , 61.2°; Mach 0.8; normalization constant, 6.96/12 000 revolution.

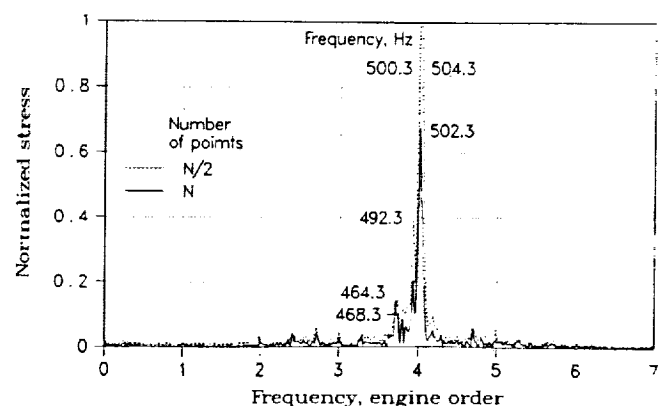


Figure 12.- Blade-tip stress spectra at 7512 rpm: blade setting angle, β , 61.2°; Mach 0.8; normalization stress, 7.14 kN/cm² (channel 4).

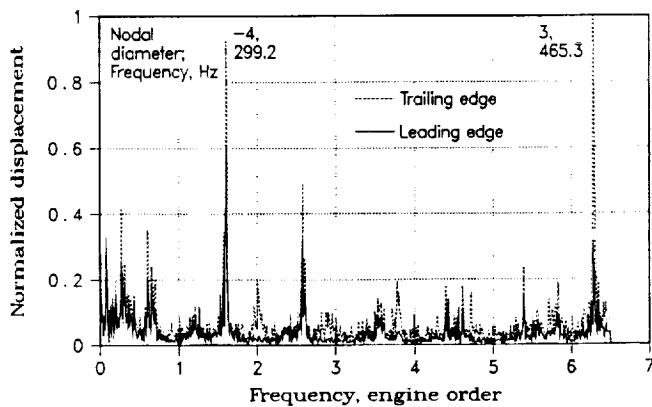


Figure 13.- Displacement spectra at 7505.6 rpm: blade setting angle, β , 61.2°; Mach 0.8; normalization constant, 5.368/12 000 revolution.

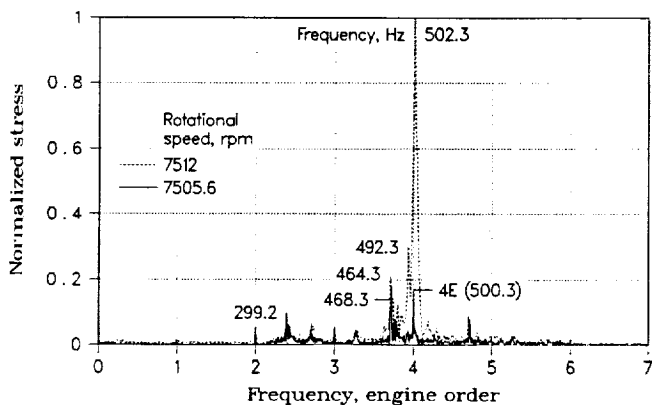


Figure 14.- Blade-tip stress spectra at 7512 and 7505.6 rpm: blade setting angle, β , 61.2°; Mach 0.8; normalization stress, 4.84 kN/cm² (channel 4).

as for Figs. 11 and 12.) The corresponding strain gage spectrum is plotted as a solid line in Fig. 14, superimposed on the 7512-rpm spectrum (dashed line). The 4.012 E, 502.3-Hz mode could not be detected in the strain gage spectrum in Fig. 14. Instead, there was a noticeable response at 4 E frequency and nonintegral responses at 2.39 E and 3.72 E corresponding to frequencies of 299.2 Hz and 465.2 Hz (essentially overlapping the 464.3-Hz peak). The two associated peaks in the displacement spectra (Fig. 13) are at 6.28 E and 1.61 E. They are folded about 6.5 E and 0 E, respectively, and correspond to nodal diameters of 3 and -4. As expected, the response associated with 4 E frequency in the strain gage spectrum is absent in Fig. 13. (Because of the -4-nodal-diameter phase required by the 4 E forced excitation, this response would be expected at 0 E.)

The raw stress levels at these two rotational speeds are illustrated in Figs. 15 and 16. The signal was clipped beyond 0.4 sec in the last figure because the tape recorder amplifier saturated. The analysis did not include the interval beyond the clipping point. (Even if the signals were not clipped, it would probably not be wise to include any appreciable portion of the high-amplitude region, as it is uncertain at which point the autosutdown started to affect the flutter amplitude.)

In order to indicate the frequency content during the spontaneous growth period for this flutter point,

an additional stress spectrum was obtained covering only the second half of the time period that is associated with the first spectrum. This resulted in half the resolution of the previous spectrum but gave more weight to the higher stress data sampled near the end of the interval. The two spectra are compared in Fig. 12. The peak response for the second (N/2) spectrum is split evenly between the two frequency lines. By using Braun's interpolation rule (Kurkov, 1984) we can conclude that the frequency for this sampling period is centered about 502.3 Hz and that the true amplitude is about 1.4 times higher than the shown peak height. On the other hand, the flutter peak associated essentially with 464.3 Hz (3.71 E) remained the same, and hence this mode did not participate in the spontaneous growth. It appears that the frequency band associated with the growth of the stress extends about 0.2 E on either side of the 4 E frequency.

Another example that includes spontaneous flutter growth is given in Figs. 17 and 18. For this point both rotors were installed. The rotational speeds for the forward and aft rotors were 8052.5 and 6397 rpm, respectively, and the corresponding blade setting angles were 58.1° and 58.6°. The tunnel Mach number was 0.7 and the relative tip Mach number was 1.033. Again, the time domain for spectral analysis extended up to the instant when the strain gage signal was clipped. The peaks at 3.97 and 3.58 E (or 532.3 and 481.3 Hz) in Fig. 18 correspond to -2 and 0 nodal diameters, respectively (Fig. 17). From the leading- and trailing-edge spectra in Fig. 17, it follows that the mode shapes associated with these two peaks are reasonably close.

In order to determine which of the two modes is responsible for the spontaneous amplitude growth, similarly as before, the spectral analysis was repeated

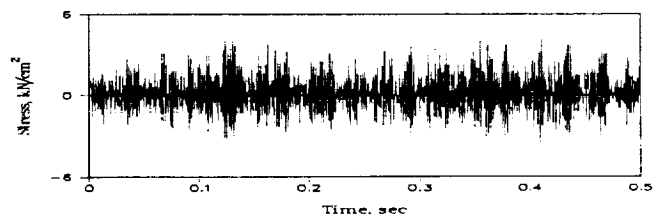


Figure 15.- Blade-tip stress (channel 6) at 7505.6 rpm: blade setting angle, β , 61.2°; Mach 0.8.

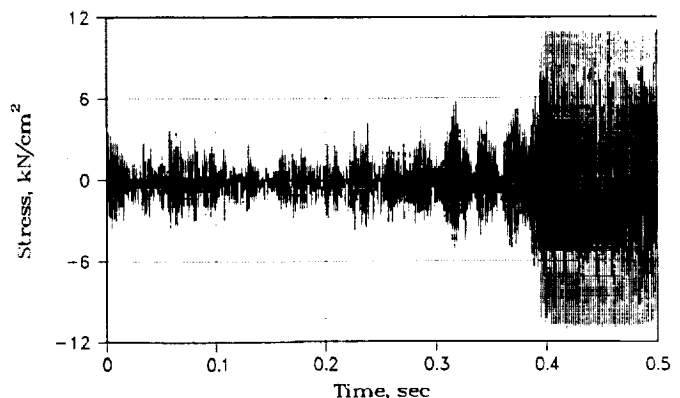


Figure 16.- Blade-tip stress (channel 6) at 7512 rpm, showing spontaneous flutter (beyond 0.4 sec signal is clipped): blade setting angle, β , 61.2°; Mach 0.8.

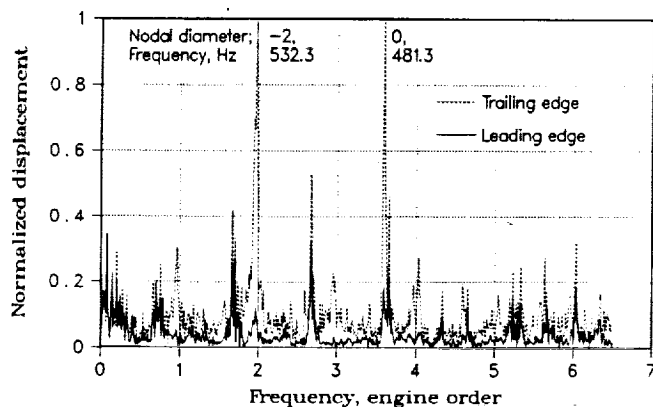


Figure 17.- Dual-rotor displacement spectra: blade setting angles, β , 58.1° (forward) and 58.6° (aft); Mach 0.7; rotational speeds, 8052.5 rpm (forward) and 6397 rpm (aft).

including only the last $N/4$ fraction of the original N -point time domain ($N = 8192$). Comparison of the spectra in Fig. 18 shows that the 3.97 E mode and the region of about 0.2 E on either side of it experienced growth, whereas the 3.59 E mode was virtually unaffected.

The spontaneous growth of flutter amplitude was noticed only for -1 and -2 nodal diameters. For the -1 nodal diameter, the additional requirement is that the relative tip Mach number be higher than 1. (No points of significant stress level occurred below this Mach number for -2 nodal diameters.) For the -2-nodal-diameter mode, rapid spontaneous flutter growth occurred for the five points closest to the 4 E frequency (Fig. 9), the two dual-rotor $\beta = 58^\circ$ points, the two single-rotor $\beta = 58^\circ$ points, and the one $\beta = 61.2^\circ$ point. The flutter growth was more gradual for the two $\beta = 61.2^\circ$ points farther from 4 E.

For the remaining flutter points, no spontaneous amplitude growth was encountered up to about the 6-kN/cm² level, when the test would usually terminate. (On a few occasions, however, the test was terminated at a lower stress level.) Regardless of whether or not spontaneous growth was observed, corresponding to each flutter point there was always a region of a low-stress-level response with one or several well-established traveling waves that could be observed in the displacement spectrum and could be maintained indefinitely. It appears, therefore, that a limit cycle sets in virtually at the flutter inception and that the observed rapid spontaneous growth is a transition to a higher amplitude limit cycle (provided that the blade does not fail). This suggests that nonlinearities have a role, not only in limiting the amplitude, but also in its growth.

Because only the low ends of the strain gage spectra were displayed in the figures, the higher harmonics fell beyond the displayed range of frequencies. However, these harmonics were clearly visible in all the linear spectra. At high stress level for the second flutter mode, the second harmonic was observed to be about one-third of the first. The stress wave shape was somewhat triangular. The second harmonic in the displacement spectra was much less significant but was observed in some spectra at twice the nodal diameter of the first.

Space limitations do not allow presentation of spectral results for all points; however, the two flutter points for which the detailed results were presented were selected to illustrate some of the more

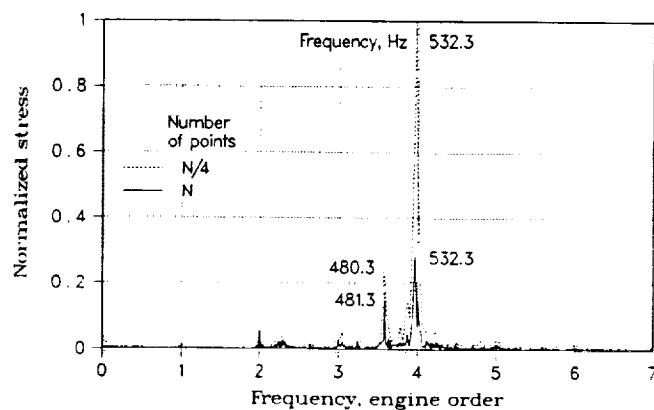


Figure 18.- Dual-rotor stress spectra (channel 12): blade setting angles, β , 58.1° (forward) and 58.6° (aft); Mach 0.7 rotational speeds, 8052.5 rpm (forward) and 6397 rpm (aft).

complicated features associated with the particular flutter mode, as well as to illustrate the method of analysis to deal with these complexities.

CONCLUDING REMARKS

Flutter blade vibrations at the near-tip span were successfully measured and monitored during a wind tunnel test of an Unducted Fan model by an optical method. The method relies upon the chopping of the laser beam by the blades rather than upon the reflection of a light beam by the blade tips. The traveling-wave nodal diameter modes were determined from the overall displacement spectra given the frequency, which was measured by strain gages. Because of the presence of mistuning, and because of the incomplete strain gage coverage of the rotor blades, this information would have been difficult, if not impossible, to obtain from the strain gage data alone.

Two distinct flutter modes were present. One was associated with the first natural mode and the other with the second. An indication of a flutter mode shape was obtained from the displacement data as the ratio of the leading- to trailing-edge flutter amplitudes. For each mode this ratio was in the neighborhood of the corresponding calculated value obtained from a finite element code that accounted only for centrifugal loads. For both modes, however, the experimentally determined amplitude ratios were lower and frequencies were somewhat higher than the calculated values. The frequency spread for the first flutter mode for the range of nodal diameters encountered in the test was relatively small; however, it was rather large for the second flutter mode, particularly for the -2-nodal-diameter group, which also occurred at a high relative Mach number. For this traveling-wave mode, most flutter points occurred close to the 4 E frequency. Past a certain flutter amplitude level, rapid spontaneous amplitude growth was observed for these points. In addition to the well-defined flutter frequency peak, the amplitude growth was also evident in a frequency band of about 0.2 E on either side of 4 E. The 4 E forced response was evident in the strain gage spectra away from the flutter region. Its source is unknown. For the high tip relative Mach numbers, spontaneous growth was also observed for the -1-nodal-diameter group. The second-flutter-mode points corresponding to the zero nodal diameter occurred at the lower relative Mach numbers and were all close to the second natural frequency.

Some evidence of secondary response at nonintegral engine orders was noticed and associated with the positive interblade phase angles at frequencies that were, in general, close to the second natural mode but with a much higher leading- to trailing-edge amplitude ratio. This ratio was essential in sorting out these points.

For both flutter modes, high incidence was found to be destabilizing.

REFERENCES

- Balan, C., Sullivan, T., Frost, R., Hoff, G., Janardan, B., and Whitfield, C., 1988, "Modern Counterrotating Blade Concepts Performance Testing in NASA Wind Tunnels," Report GE TM87-528, NASA Contract NAS3-24080.
- Bendiksen, O.O., 1990, "Aeroelastic Problems in Turbomachines," AIAA Paper No. 90-1157-CP.
- Crawley, E.F., and Ducharme, E.H., 1989, "Parametric Trends in the Flutter of Advanced Turboprops," ASME Paper No. 89-GT-280.
- Kaza, K.R.V., Mehmed, O., Narayanan, G.V., and Murthy D.V., 1987, "Analytical Flutter Investigation of a Composite Propfan Model," NASA TM-88944 (also, AIAA-87-0738).
- Kurkov, A.P., 1988, "Optical Measurement of Propeller Blade Deflection," NASA TP-2841.
- Kurkov, A.P., 1989, "Optical Measurement of Unducted Fan Blade Deflections," ASME Paper No. 89-GT-298, ASME Journal of Turbomachinery, Vol. 112, 1990, No. 4, pp. 751-758.
- Kurkov, A.P., 1984, "Formulation of Blade-Flutter Spectral Analyses in Stationary Reference Frame," NASA TP-2296.
- Mehmed, O., and Kaza, K.R.V., 1986, "Experimental Classical Flutter Results of a Composite Advanced Turbo-prop Model," NASA TM-88792.
- Nieberding, W.C., and Pollack, J.L., 1977, "Optical Detection of Blade Flutter in YF-100 Turbofan Engine," ASME Paper No. 77-GT-66 (NASA TM X-73573).
- Podboy, G.G., and Krupar, M.J., 1989, "Laser Velocimeter Measurements of the Flow Field Generated By an Advanced Counterrotating Propeller," AIAA Paper No. 89-0434.
- Singleton, R.C., 1969, "An Algorithm for Computing the Mixed Radix Fourier Transform," IEEE Transactions, Audio and Electroacoustics, Vol. AU-17, No. 2, pp. 93-103.
- Whitehead, D.S., 1966, "Torsional Flutter of Unstalled Cascade Blades at Zero Deflections," Report ARC-R&M-3429, British Aeronautical Research Council, London, England.

Report Documentation Page

1. Report No. NASA TM-103285		2. Government Accession No.		3. Recipient's Catalog No.	
4. Title and Subtitle Optical Measurement of Unducted Fan Flutter				5. Report Date	
				6. Performing Organization Code	
7. Author(s) Anatole P. Kurkov and Oral Mehmed				8. Performing Organization Report No. E-5741	
				10. Work Unit No. 505-63-1B	
9. Performing Organization Name and Address National Aeronautics and Space Administration Lewis Research Center Cleveland, Ohio 44135-3191				11. Contract or Grant No.	
				13. Type of Report and Period Covered Technical Memorandum	
12. Sponsoring Agency Name and Address National Aeronautics and Space Administration Washington, D.C. 20546-0001				14. Sponsoring Agency Code	
15. Supplementary Notes Prepared for the Thirty-sixth International Gas Turbine and Aeroengine Congress and Exposition, Orlando, Florida, June 3-6, 1991.					
16. Abstract The paper describes a nonintrusive optical method for measuring flutter vibrations in unducted fan or propeller rotors and provides detailed spectral results for two flutter modes of a scaled unducted fan. The measurements were obtained in a high-speed wind tunnel. A single-rotor and a dual-rotor counterrotating configuration of the model were tested; however, only the forward rotor of the counterrotating configuration fluttered. Conventional strain gages were used to obtain flutter frequency; optical data provided complete phase results and an indication of the flutter mode shape through the ratio of the leading- to trailing-edge flutter amplitudes near the blade tip. In the transonic regime the flutter exhibited some features that are usually associated with nonlinear vibrations. Experimental mode shape and frequencies were compared with calculated values that included centrifugal effects.					
17. Key Words (Suggested by Author(s)) Flutter Aeroelasticity Blade vibrations			18. Distribution Statement Unclassified - Unlimited Subject Category 07		
19. Security Classif. (of this report) Unclassified		20. Security Classif. (of this page) Unclassified		21. No. of pages 10	
				22. Price* A03	